HHS Public Access

Author manuscript

Nat Biomed Eng. Author manuscript; available in PMC 2022 October 11.

Published in final edited form as:

Nat Biomed Eng. 2022 May ; 6(5): 559–568. doi:10.1038/s41551-022-00876-4.

Prospective testing of clinical Cerenkov luminescence imaging against standard-of-care nuclear imaging for tumour location

Edwin C. Pratt[1,2,3], **Magdalena Skubal**[2,3,&], **Benedict Mc Larney**[2,3,&], **Pamela Causa-Andrieu**[3,&], **Sudeep Das**[2,3], **Peter Sawan**[3], **Abdallah Araji**[3], **Christopher Riedl**[3], **Kunal Vyas**[4], **David Tuch**[5], **Jan Grimm**[1,2,3,6,*]

[1]Pharmacology Department, Weill Cornell Medical College, New York, NY, 10065, USA.

[2]Molecular Pharmacology Program, Memorial Sloan Kettering Cancer Center, New York, NY, 10065, USA.

[3]Department of Radiology, Memorial Sloan Kettering Cancer Center, New York, NY, 10065, USA.

[4]Lightpoint Medical Ltd., Waterside, Chesham, HP5 1PE, UK.

[5]Lightpoint Medical Inc., Cambridge, MA, 02139, USA.

[6]Department of Radiology, Weill, Cornell Medical Center, New York, NY, 10065, USA.

Abstract

In oncology, the feasibility of Cerenkov luminescence imaging (CLI) has been assessed by imaging superficial lymph nodes in a few patients undergoing diagnostic ^{18}F-FDG positron emission tomography / computed tomography (PET/CT). However, a weak luminescence signal required the removal of ambient light. Here, we report the development of a clinical CLI fiberscope with a lightproof enclosure, and the clinical testing of the setup using five different radiotracers. In an observational prospective trial (ClinicalTrials.gov identifier NCT03484884) involving 96 patients with existing or suspected tumours with nodal metastases and scheduled for routine clinical FDG-PET or ^{131}I therapy, the level of agreement of CLI and standard-of-care imaging (PET or planar single-photon emission CT) for tumour location was ‘acceptable’ or higher (≥ 3 in the 1-to-5 Likert scale) for 90% of the patients. CLI correlated with the

*Correspondence and requests for materials should be addressed to Jan Grimm, grimmj@mskcc.org.

&These authors contributed equally

Author contributions

ECP, MS, BML, SD, PC, and JG imaged patients, analysed the data, and wrote this manuscript. DT and KV and designed and constructed the fiberscope camera and enclosure and wrote the manuscript. CR read and identified patients for consent in addition to PC, JG, AA, and PS, who graded Cerenkov luminescence images with Likert scores and wrote the manuscript. We thank Rebecca Teng, Ryan Min, Frank Avalone, and Nayab Shahid for consenting and managing patients for NCT03484884. We thank Andre Platzman, Lukas Carter, and Samuel Hellman in the Department of Medical Physics for their phantom, fiberscope arm, and angular dependence holder designs.

Supplementary information The online version contains supplementary material available at https://doi.org/10.1038/s41551-01X-XXXX-X.

Reporting summary

Further information on research design is available in the Nature Research Reporting Summary linked to this article.

concentration of radioactive activity, and captured therapeutically relevant information from patients undergoing targeted radiotherapy or receiving the alpha emitter ^{223}Ra, which cannot be feasibly imaged clinically. CLI could supplement radiological scans, especially when scanner capacity is limited.

Prospective testing of a clinical fiberscope with a lightproof enclosure for Cerenkov luminescence imaging using five different radiotracers showed satisfactory agreement with standard-of-care nuclear imaging for tumour location.

According to the World Nuclear Association, more than 40 million nuclear-medicine procedures are performed each year, and about one in 50 people in developing countries use diagnostic nuclear medicine annually[1]. Approximately 70% of cancer deaths worldwide occur in low-to-middle-income countries, yet only 30% of low-income countries can offer treatment services[2]. The majority of these new cases will be lung, breast, and abdominal (liver, stomach and colorectal) cancers that require some form of imaging. Of the nuclear medicine modalities currently available, positron emission tomography (PET) is a widely accepted diagnostic tool. However, PET requires dedicated infrastructure for isotope supply, with only 10% of countries having at least one scanner per million population[3] with recent guidance for enhancing global access to nuclear imaging[4,5]. For example, India has 0.08 PET scanners per million people[6] and Latin America has 0.3 per million, compared to 7 scanners per million in the US[7]. Only 14% of developing countries have at least one CT scanner per million population. Furthermore, PET is considered a specialized instrument with exam fees ranging from $1,000-$2,500 in the US and costs varying in other countries[8] based on insurance coverage and radioisotope availability. While longer-lived radiopharmaceuticals such as Iodine-131 can be shipped or shorter-lived isotopes such as Gallium-68 can be produced locally with specialized generator systems[9]. Surveys from several nations confirmed the use of Gallium-68 generators in 13 of 32 countries while the use of Iodine-131 was available in 30 of the 32 countries[4]. Access to lower-cost isotope sources and scanners represent an unmet and growing need for nuclear clinical imaging in both developing and established medical networks.

Numerous radionuclides for therapy, PET, and single photon emission computed tomography (SPECT) are of sufficient energy for use in Cerenkov luminescence (CL) imaging (CLI)[10,11]. CL is generated by a charged subatomic particle traveling at a velocity exceeding the speed of light in a dielectric medium, like tissue. The amount of light produced is proportional to the particle energy and refractive index of the medium[12,13] and the emission spectrum is UV-weighted and continuous through the visible spectrum with the intensity decreasing relative to $1/\lambda^2$. CL is emitted from numerous radioisotopes present within the targeted tissue, and due to the high degree of scattering, no angular dependence of emitted CL is observed[14]. The intensity of CL detected is based on isotope photon yield, activity present in the tissue, depth of that tissue and optical properties of the tissue along the emitted photons path from its source. Optical imaging technologies such as CLI can achieve mesoscale resolution due to recent advances in camera technology, and new probes can convert Cerenkov emission to longer (red-shifted) penetrating wavelengths[13,15,16]. These advances have enabled CLI to emerge in preclinical[17,18], *ex vivo* clinical, and proof-of-principle clinical settings[19–21] for potential tumour detection. The portability of CL cameras

combined with the array of available theranostic radiotracers suggests an affordable new nuclear imaging modality[22] for basic disease surveillance and therapy monitoring.

Our prior pilot study reported the correlation in nodal uptake of patients administered with the radiotracer ^{18}F-fluoro-2-deoxyglucose (^{18}F-FDG) between CL and PET imaging, with the latter being received as the standard of care[19]. Superficial lymph nodes were imaged in 6 patients as the first CLI trial (NCT01664936). This trial highlighted that CLI is specific, though with an extremely weak signal, requiring ambient light removal to avoid overpowering of the weak CL. The previous generation setup required switching off all light sources even outside the room along with the sealing of any light emitting electronics in the room and the door[19]. This setup ultimately caused safety and operational shortcomings for patients and employees alike. For further clinical investigation of CLI, a more versatile and standardized imaging system was needed.

Based on our previous CLI clinical trial experience, we have developed a clinical-grade, fiberscope-equipped camera based on an *ex vivo* CLI system. This work examined the feasibility of this unique system to capture CL directly from patients. Previous reports have shown *ex vivo* imaging systems to successfully image positron-emitting isotopes for post-resection margin confirmation in a dark box configuration[23–27]. Adding a fiberscope enhanced camera manoeuvrability but came at the cost of reduced signal capture through the fibre, artifacts from scintillation within the fibre and a reduced field of view thus requiring a binning dependent acquisition time on the order of 5–15 minutes[28,29]. To limit scintillation, a metal (lead) cerrobend baffle was created and installed at the front of the fiberscope. Remaining scintillation and gamma strikes were further removed during image post processing via outlier removal in ImageJ (median filtering). To improve the CL signal-to-noise through exclusion of ambient light, we implemented a clinical lightproof enclosure (Fig. 1, Extended Data Fig. 1). The enclosure isolated the imaging procedure from external light sources, lowered image noise and provided greater imaging space for patients with claustrophobia, extreme obesity, or limited mobility.

Preclinical testing of the camera and enclosure was conducted to ensure the feasibility of the system covering image uniformity and confirming lightproof performance of the clinical enclosure (Supplementary Fig. 1). Linearity and sensitivity of the fiberscope camera was tested with titrations of $^{68}GaCl_3$ and ^{18}F-FDG and the use of optical filters and tissue phantoms to distinguish depth (Supplementary Fig. 2). Using a calibrated light source, the limit of detection for the CLI fiberscope was determined to be 0.03 pW (Supplementary Fig. 3a–b) while the effects of binning on resolution were determined using a resolution target with an achievable resolution of 200μm, 400μm and 1mm for 1×1, 4×4 and 8×8 binning, respectively (Supplementary Fig. 4). The spatial resolution of the developed CLI system is comparable to the resolution of clinical PET systems, however as is common with optical imaging systems this resolution dramatically decreases at increased tissue depths[30]. *Ex vivo* imaging of mice confirmed linearity for CLI in tissue, and the utility of a selection of filters with short bandpass and long pass emissions for spectral imaging (Supplementary Fig. 5). We next tested the degree of scintillation in the fiberscope with a ^{18}F-FDG source (Supplementary Fig. 6a–b) and the benefit provided by lead shielding around the detector (Supplementary Fig. 6c), as high activity amounts were planned for patients receiving

therapeutic doses of Iodine-131 and Lutetium-177. Having determined the fiberscope system was lightproof and could capture CLI across a range of intensities in tissue, the system was ready for clinical testing with patients.

Several radiopharmaceuticals are available in nuclear medicine clinics (Table 1) for PET and SPECT imaging, but they require dedicated, costly and time-consuming imaging systems. Therapies such as $^{223}RaCl_2$ currently do not even have a feasible imaging method (1% gamma emission, several day clearance[31], requiring the additional radiotracer ^{18}F for correlative imaging) but are detectable with CLI (Supplementary Fig. 6d–e). The radiopharmaceuticals shown in Table 1 emit CL at varying intensity levels and are administered in different quantities. All these radiopharmaceuticals were imaged in patients with our fiberscopic CLI system.

We searched original articles published in English from Jan 1, 2009 to Dec 17, 2020 for clinical studies including the term “Cerenkov.” Prior clinical studies have shown single-digit case reports of Cerenkov imaging of superficial tumours consisting of thyroid[20], colon[28] (contact mode only), arm axilla[19], and *ex vivo* imaging of resected specimens[25–27,46,48]. Of the trials directly imaging patients, one study imaged a single patient, while the only other clinical trial report imaged 6 patients. These studies focused on proof-of-principle imaging with single radiotracers, and without a lightproof enclosure.

Results

Between May 2018 and March 2020, 96 patients consented and were imaged with the Cerenkov fiberscope. Of the 96 patients consented, 106 imaging sessions were conducted with the five radiopharmaceuticals as detailed in Table 1. Patients were 42% female and 58% male, with a median age of 58.2 (26–87) years old. Concerning race, 78% were white, 9% Black or African American, 6% Asian, and 7% unknown; in terms of ethnicity, 11% identified as Hispanic. Thirteen patients were available for subsequent imaging sessions, allowing for longitudinal surveillance of therapy (eight ^{177}Lu-DOTATATE (DOTA-(Tyr^3)-octreotate), four ^{68}Ga/^{177}Lu-DOTATATE, and one ^{18}F-FDG).

Imaging feasibility and efficacy.

CLI was feasible using a fiberscope attachment with all five radiotracers tested in the protocol (Table 1). A total of 96 patients were imaged, of which 13 patients participated in serial imaging sessions tracking their therapy. Three of the five radiotracers tested (^{18}F-FDG, Iodine-131, and ^{177}Lu-DOTATATE) had a highly significant correlation with CLI intensity and quantified activity delivered to the region. The remaining two radiotracers had positive though non-significant correlations, likely due to varied tissue avidity for the tracer along with tissue absorbance and scattering of light. Fiberscopic CLI identified the most superficial and avid lesions. A Likert scale was used to compare CLI to standard-of-care nuclear imaging (PET, SPECT and planar imaging) with averaged scores from four board-certified radiologists. Likert ranking[32–35] yielded 90% with an average score of 3–5 (acceptable to high agreement) and 26% scored 4–5 (good to high agreement) between CLI and standard-of-care imaging. The Likert analysis can be found in Table 2 and is organized by radiotracer detailing the number of imaging sessions, summary scores, and percentage.

Overall, patients could be imaged with Iodine-131, Fluorine-18, Gallium-68, Lutetium-177, and Radium-223 using the fiberscopic CLI system with activity ranges observed of 27–200 mCi (1.0–7.4 GBq), 10–14.9 mCi (0.37–0.55 GBq), 4.4–5.5 mCi (119–149 GBq), 188–200 mCi (6.9–7.4 GBq), and 0.091–0.177 mCi (0.0033–0.0065 GBq), respectively.

CLI of radioiodine therapy.

Of the 96 patients, 25 were administered Iodine-131 to identify uptake in the thyroid bed and possible distant disease; this was the first subset of patients to be imaged by this CLI setup. Of these images, 80% (score 3–5) and 36% (score 4–5) agreed with the standard-of-care SPECT scans. The resulting CL image (false colorized with the Cyan Hot look up table (LUT) in ImageJ, Fig. 2a) shows focal uptake in the thyroid bed as seen on the SPECT scan.

CLI of tumour hypermetabolism.

Of the 20 patients receiving ^{18}F-FDG for staging and monitoring of lesions, 75% (score 3–5) and 40% (score 4–5) agreed with lesion locations as defined by PET. In one patient's neck, CLI identified a single large focal area on the right side (Fig. 2b), appearing as one region due to light scatter and post-processing steps compared to the PET/CT scan.

CLI of neuroendocrine tumours.

In a cohort of 28 patients administered ^{68}Ga-DOTATATE, one of the brightest CLI radionuclides used in this study[13], CLI also identified lesions present in the abdomen, in spite of the significantly greater depth. Of these lesions, 89% (score 3–5) and 11% (score 4–5) agreed with lesion locations as defined by PET, though tumour depth and retention in the spleen increased the complexity of image interpretation (Fig. 2c).

CLI of neuroendocrine tumour radiotherapy.

For eligible ^{177}Lu-DOTATATE patients receiving therapy, high therapeutic doses of 200 mCi (7.4 GBq) allowed fiberscopic CLI despite the low CL emission of ^{177}Lu. Of the 26 ^{177}Lu-DOTATATE patients receiving therapy, 81% (score 3–5) and 19% (score 4–5) of the images agreed with planar gamma scans of the whole patient. After the first cycle of ^{177}Lu-DOTATATE, posterior CLI showed focal activity on the spine of one patient (Fig. 2d), whilst the 2D planar scan showed radiopharmaceutical uptake in the liver and thoracic and abdominopelvic nodes, as well as the spine.

CLI of metastatic prostate cancer radiotherapy.

Patients with metastatic castration-resistant prostate cancer were given ^{223}Ra (Xofigo®) as part of their standard-of-care therapy with a subsequent ^{18}F bone scan the following month to monitor disease burden. Of the seven patients receiving $^{223}RaCl_2$, 71% (score of 3) and 0% (score 4–5) of the images agreed with known lesion locations from prior Na^{18}F scans. $^{223}RaCl_2$ is cleared through the gastrointestinal tract over several hours[36] in addition to bone uptake as a calcium mimetic. Patients imaged within one hour of receiving $^{223}RaCl_2$ have a combination of physiologic distribution, degenerative bone uptake, and potential metastatic lesions, making definitive identification by CLI in this time window unlikely without extensive imaging knowledge. In a representative patient, a prior Na^{18}F

PET scan identified radiopharmaceutical uptake within the pelvic bone and fourth left rib, as well as in degenerative lesions in the cervical spine (Fig. 2e). CLI was focused on the degenerative lesions in the cervical spine from a posterior position. Here, CLI could directly capture $^{223}RaCl_2$ uptake without a subsequent $Na^{18}F$ or ^{99m}Tc bone scan, though physiologic distribution and uptake of $^{223}RaCl_2$ in degenerative lesions by the tracer itself complicates a potential diagnosis by any imaging modality alone without a biopsy.

Representative Cerenkov images for $Na^{131}I$ thyroid therapy, ^{18}FDG lymphoma imaging, ^{68}Ga-DOTATATE imaging, ^{177}Lu-DOTATATE therapy, and $^{223}RaCl_2$ therapy can be found in Fig. 2 with additional patient images for each radiotracer (Extended Fig. 2) and imaging angle (Extended Fig. 3). The patients' corresponding standard-of-care images are shown and highlight the versatility of the clinical Cerenkov fiberscope to image numerous radiopharmaceuticals with different emission types and levels. Several subsequent phantom images were acquired with a higher binning mode (8×8), yielding similar images in 2–5 minutes compared to 15 minutes (4×4) (Supplementary Fig. 7). By increasing the binning, imaging time could be reduced with a nominal loss in resolution dependent upon the binning level at the imaging distance of 1.4' since the post processing macro includes steps of image smoothing. Importantly, the angular dependence of the camera performs best in the planar view (0°), with lower intensity and greater image deviations when imaged at an angle between 0° and ±45° (Supplementary Fig. 8). Images acquired as part of this study were done as close to the planar view to the patients' area of interest as patient comfort would permit.

Spectral Cerenkov Luminescence Imaging.

CL is a continuous UV-weighted spectrum of emitted light. However, much of this UV and blue light (below 600nm) is absorbed (predominantly by haemoglobin) and scattered (predominantly by lipids) by the known optical properties of biological tissue[37]. Light with wavelengths above 600 nm (red light) undergoes reduced scattering and absorption in tissue and thus is better at penetrating tissue[11,37]. This is highlighted by the notable success of indocyanine green and infrared dyes for near infrared image-guided surgery[38–40], though fluorescein examples, emitting in the 500–600nm range have also shown significant clinical benefit and utilization[41,42]. We installed a series of filters on a filter wheel with a selection at spectral bands <500 nm, between 500–550 nm, 550–600 nm, and >600 nm, with the intent of segmenting the emitted CL light to understand lesion complexity. Patients with known complex or deep lesions were imaged with the additional filters for fifteen minutes per filter (4×4 binning) for a total imaging session of 75 minutes. One patient with multiple lymphoma lesions in the left neck presented with multiple ^{18}F-FDG-avid lesions spanning from the lower neck into the supraclavicular region (level IV and VB) on PET/CT (Fig. 3a). CLI with an open filter revealed a spread of signal across the neck whereas the 600nm long-pass filter presented two clearer areas of CL emission. CLI filters below 600nm (Extended Fig. 4) did not provide any additional definition of the nodules in the supraclavicular region, as the CLI seen is mainly longer red-shifted at wavelengths greater than 600nm[11,43,44]. Of all the lesions seen by PET/CT and represented in the MIP (Fig. 3b), lesion 1 and lesion 3 are of similar size and SUV, yet lesion 1 is deeper (Fig. 3c). Looking at the 600nm image, the less intense lesion is lesion 1. Similar filter performance was confirmed with

a phantom containing five spheres filled with ^{18}F-FDG at varying depths (Supplementary Fig. 9) as well as two additional patients administered Iodine-131 or ^{177}Lu-DOTATATE (Extended Fig. 4). Future filtering of CL light in patients for screening should be focused on wavelengths above 600nm as the 600nm long-pass filter best agreed with the expected CLI intensity for the combination of lesion intensity and depth as measured by PET/CT.

Therapy monitoring.

As CL can be used to image a variety of radiotracers in patients, it could be used to track targeted radiotherapy to evaluate therapy progress and approximate the administered dose. Throughout this clinical trial, 11 patients with neuroendocrine tumours underwent ^{177}Lu-DOTATATE peptide receptor radionuclide therapy (PRRT) and consented to multiple CL imaging sessions, thereby providing the opportunity to see changes in CLI over the course of therapy. As theranostic pairs, ^{68}Ga-DOTATATE and ^{177}Lu-DOTATATE represent 10 of the 11 CLI pairs. One patient was imaged in four sessions over one year to show therapy progress by CL, comparing CL images over time at the same location, distance, and image settings to the original radiotracer scan. This representative patient was diagnosed with well-differentiated pancreatic neuroendocrine tumour metastatic to the liver, on treatment with PRRT. Baseline ^{68}Ga-DOTATATE (Fig. 4a, **top**) fused PET/CT images delineate a DOTATATE-avid tumour in the pancreatic body and multiple liver metastases. CLI of the patient immediately post-PET/CT scan shows a central abdominal lesion (Fig. 4a, **bottom**). During PRRT, the first cycle shows ^{177}Lu-DOTATATE uptake in the liver and pancreatic tumour by planar scintigraphy (Fig. 4b, **top**). CLI of the abdomen correlates ^{177}Lu-DOTATATE in the liver with the scintigraphy (Fig. 4b, **bottom**). After the third cycle of PRRT, the 2D planar scintigraphy image (Fig. 4c, **top**) shows a reduction in radiopharmaceutical uptake in the pancreas and liver. The corresponding CLI scan (Fig. 4c, **bottom**) shows no CL signal from that anatomical region (Fig. 4b). After the completion of all PRRT cycles, a diagnostic scan with ^{68}Ga-DOTATATE PET/CT (Fig. 4d, **top**) delineates a marked reduction in DOTATATE uptake at the site of the pancreatic tumour and resolved uptake in the liver metastases, which was matched again by the CL image, which also didn't show appreciable activity (Fig. 4d, **bottom**). CL images with a wider intensity range were also produced to exclude any appreciable CL signal for residual disease (Extended Fig. 5).

Cerenkov Luminescence intensity analysis

In this study, each CL patient image was analysed and compared to clinical PET or planar SPECT scans to determine any CL intensity correlation with lesion avidity and lesion depth. A line has been added to each graph in Fig. 5 to represent the limit of detection established by the camera electrical and read noise level. Patients receiving ^{18}F-FDG, had a highly significant correlation for CL intensity with radioactivity present in the imaging region (Fig. 5a) and a limit of detection of 0.05 μCi/mL (2 kBq/mL) for the imaging region. As expected, due to the optical properties of tissues, CL intensity decreased significantly with increasing lesion depth[37] (Fig. 5b). For patients receiving ^{131}I, administered activity 100–200 mCi (3.7–7.4 GBq), iodine deposited in the thyroid bed was measured by planar SPECT between 3 and 6 days post administration 0.058–9.64 mCi (0.0021–0.36 GBq). A significant correlation between CLI intensity and deposited activity was observed with a

limit of detection of ~ 60 μCi (2.2MBq) in the thyroid bed (Fig. 5c). CLI intensity was not found to have a significant correlation with lesion depth (Fig. 5d), potentially due to the scattering and absorption of light, the wide range of activity present in patient thyroid beds and the location of lesions. One of the brightest radionuclides for CLI, ^{68}Ga, offered the possibility for imaging deeper lesions in the abdomen with an average of 5.3 mCi (0.2 GBq) administered per patient. ^{68}Ga-DOTATATE Cerenkov intensity was spread across a four-fold difference between all patients imaged and did not significantly correlate with measured activity concentration (Fig. 5e), or lesion depth (Fig. 5f). This variance in ^{68}Ga-DOTATATE Cerenkov intensity was potentially due to the lesions being located deep in the abdomen, even inside the liver, which would highly attenuate all optical signal with previous estimates of Cerenkov emission being limited to the first two centimetres of tissue[45]. As a theranostic pair, patients with avid uptake of ^{68}Ga-DOTATATE were eligible for ^{177}Lu-DOTATATE therapy. Patients received an average 195 mCi (7.2 GBq), with 36–86 mCi (1.3–3.2 GBq) deposited into tumours within the abdominal cavity. CL intensity was highly correlated with total activity deposited within the abdomen (Fig. 5g) with a limit of detection of about 40 mCi (1.5GBq) of ^{177}Lu. However, no significant correlation for lesion depth was determined (Fig. 5h). Lastly, $^{223}RaCl_2$ CL intensity could not be correlated due to insufficient number of patients with Na^{18}F or ^{99m}Tc-MDP scans including depth of lesions (Supplementary Fig. 10).

Discussion

CLI has recently emerged as an optical technique to image radiopharmaceuticals, and proof of principle examples have been established in preclinical models as well as clinical pilot trials[19,20,25–27,29,46]. Prior trials have shown the effectiveness of CLI for positive margin detection during resection[25–27,47–49] and the overall feasibility of imaging lymph nodes[19] or the thyroid bed[20]. This trial, the largest clinical CLI study to date, involved over 106 patient imaging sessions (96 individual patients) covering five radiotracers, of which three had never been imaged before by CLI in patients. The versatility of CLI allows patients to be triaged with short sessions (5 to 15 mins) to determine coarse radiotracer distribution, and, if distribution is abnormal, sent for a detailed but expensive PET (or SPECT) study. Similarly, patients in remission could also benefit from this modality for facile screening.

CLI suffers from commonly shared limitations in other optical modalities, such as lens aberrations along with the exponential attenuation and scattering of light by tissue with increasing depth. To counteract some of these limitations Fast Fourier Transform (FFT) bandpass image processing along with border cropping of the CLI images was carried out to reduce aberrations and vignetting imparted by the given setup[50]. The CLI setup utilized in this work incorporated a fiberscope for imaging flexibility, which has been known to reduce sensitivity up to several-fold[28,29] however, each radiopharmaceutical tested could be readily imaged with this CLI system. The main factors affecting CLI resolution and intensity compared to PET or SPECT include the scattering of light, tissue absorbance (predominantly from hemoglobin[37]), and the radiopharmaceutical's overall CL radiance. We have shown that patients receiving ^{18}F-FDG for staging can be readily imaged and patients undergoing therapy such as ^{177}Lu-DOTATATE amongst other radiopharmaceuticals. By using filters to segment a broader range of the CL spectrum, tumour multiplicity or

heterogeneity might be gleaned, warranting a wider analysis in patients without prior knowledge of lesion depth. As all CL images acquired in this study were obtained in an unblinded fashion, future blinded clinical studies are warranted. Given the heterogeneity of the tissue regions imaged, the amount of radiotracer administered, and the CL radiance by isotope[13], not every radiotracer seems suited for semi-quantitative CLI in patients. Patients receiving ^{18}F-FDG or Iodine-131 for head and neck cancers, and patients undergoing therapy with ^{177}Lu-DOTATATE performed best for CL quantification. For patients receiving ^{68}Ga-DOTATATE and Radium-223, CLI should be further investigated to determine the optimal imaging parameters for quantification. In general, methods such as external fiducial markers, CT weighting factors, and fixed imaging positions such as directly anterior or posterior to the patient would improve image comparison between sessions and with existing SPECT or PET scans. In addition, future studies need to include a greater number of patients with darker skin as this method relies heavily on the optical property of skin for signal transmission.

CL represents an affordable alternative (up to $125,000 compared to $1,500,000 for PET/CT systems) imaging modality for lower-cost molecular imaging with approved radiopharmaceuticals. A significantly cheaper imaging system will allow all hospitals and clinics to increase molecular imaging capacity and introduce a simple nuclear medicine program where previously, installation of conventional PET and SPECT systems would have been cost prohibitive. Here, CLI could be used for screening to determine physiological versus potential pathologic radiopharmaceutical uptake, serving as a rudimentary evaluation scan that can precede any more expensive and less available modality. The enclosure and camera are moveable and require minimal installation in comparison to conventional systems; thus, CLI is a molecular imaging modality that can become accessible to patient centres beyond major metropolitan hospitals provided generator systems producing $^{68}GaCl_2$ or an isotope supply chain can support this expansion. While CLI would enable more facilities to scan patients, it should be mentioned that CLI relies on the administration of a radiotracer, depositing some radiation dose to each patient. In comparison, methods such as ultrasound, optoacoustic and fluorescence would be non-ionizing, meaning CLI, is similar to nuclear imaging, and should be reserved for oncology and more time sensitive treatments. A wide range of radiotracers used in both imaging and therapy can be imaged with CLI. Given the broad interest in alpha emitters for therapy, CLI is additionally a potential imaging modality for alpha therapy monitoring. CLI provides simple and so far, single projections, imaging data at a fraction of the cost and time of traditional PET or SPECT scanners. The ease of repeated measurements with CLI can open new imaging workflows that track patient therapy when conventional imaging may not be feasible or cost-prohibitive and provides similar planar information to that of gamma cameras.

While imprecise, the intensity analysis of each radiotracer could help the clinical decision-making process. For example, patients receiving iodine therapy for thyroid cancer usually post thyroid resection, so no iodine should be observed in the neck, thus any CLI signal two-fold above noise in the neck (excluding salivary glands) would suggest the presence of residual thyroid tissue. Also, for ^{18}F-FDG, Iodine-131 and ^{177}Lu-DOTATATE the intensity significance establishes that increasing CLI intensity correlates with disease burden and or

lesion avidity, providing a crude barometer of therapy progress. In this case CLI can provide a critical tool for a physician with limited diagnostic access.

Our study has expanded the list of clinical radiopharmaceuticals imaged with CLI and provides intensity and depth analysis for each tracer. Prior studies have focused only on the absence or presence of CL[19,20], and in this study implementation of the Likert ranking system solidifies CLI location to agree across several radiotracers with standard-of-care SPECT or PET scans. Prior work has shown *ex vivo* CL correlation with PET[25–27,46], but this work correlates CLI directly with PET or SPECT in patients. Two prior studies used an endoscope, covering preclinical feasibility[29] and on contact imaging in colorectal patients[28]. We added filters to clinical CLI, with CLI above 600 nm providing the most relevant images, as tissue highly absorbs light below 600 nm, resulting in little emitted light to be meaningfully filtered[37]. Future implementations should look to compensate for the inherent scattering and absorption by tissue by correcting for tissue properties, as has been performed for dosimetry via CL[51]. However, this was outside the scope of this work and was not possible, as not all patients underwent CT scanning. Furthermore, the automation of post-acquisition processing employed here allows for open-source, unbiased image analysis by the reading radiologist for patient staging and disease surveillance during and after therapy. CLI could become a portable and less expensive radiation-based patient-screening tool. The results presented here are based on *a priori* knowledge of tumour location. Future clinical trials should aim to perform blinded imaging sessions to further establish the applicability of clinical CLI and to investigate how clinical CLI can aid in clinical diagnostics.

Fiberscopic CLI provides a unifying molecular imaging modality for nearly all radionuclides currently used in the clinic. By combining a commercially available electron multiplying charge coupled device (EMCCD) sensor into a clinical-grade enclosure equipped with a fiberscopic lens, clinical CLI can identify lesions in patients across several cancer types and radiopharmaceuticals. The versatility of the system allows broad front-line screening to identify lesion location with the intensity correlating to radioactivity present for ^{18}F-FDG, Iodine-131 and ^{177}Lu-DOTATATE radiotracers. Furthermore, filtering above 600 nm could improve the CLI of lesions. This is especially useful when conventional CT and MRI are unavailable or cost-prohibitive. While the depth penetration and quantification of PET remains superior, fiberscopic CLI with a lightproof enclosure, as designed, can serve as a method for superficial-disease surveillance, staging, and therapy response imaging. With further engineering of a patient shroud, CLI can be rapidly brought into numerous intraoperative settings for Cerenkov assisted resection.

Outlook

This report of the largest CLI study to date (96 patients, 106 imaging sessions) shows that CLI can be used for patient imaging. The study was conducted with a fiberscope for future flexible intraoperative imaging. The work used three radiotracers for Cerenkov imaging, and a lightproof enclosure allowed Cerenkov imaging without ambient-light bias. Light-intensity analysis of ^{18}F-FDG and ^{177}Lu-DOTATATE Cerenkov images correlated with measured PET and SPECT activity concentrations, respectively, and allowed for the monitoring or targeted radiotherapy. Images show superficial and deeper lesion light sources with the

addition of filters, although an approximation of lesion depth could not be inferred without a CT scan. Cerenkov imaging with the alpha emitter $^{223}RaCl_2$ allowed direct imaging of the therapeutic dose without the need for an additional bone scan.

This work emphasizes that CLI is a nuclear-imaging approach that works with a variety of tracers and at several tumour locations, at a fraction of the monetary and time costs of other modalities. CLI could provide a semi-mobile imaging modality to low-income countries where SPECT or PET implementation is cost-prohibitive. This work also highlights the limitation of CLI as an optical imaging modality that is subject to light scattering and absorption by tissue, significantly reducing image fidelity compared to gold-standard PET/CT and SPECT/CT systems. The knowledge gathered from this study could have implications for future optically based cancer-screening methods (especially for fluorescence imaging, which is far less photon-starved).

Methods

Study design and participants

This work was funded by NIH R01CA18395305. The CLI trial (ClinicalTrials.gov identifier NCT03484884) was conducted at a single recruitment site in close association with the PET/CT and nuclear medicine clinics. The study was determined by the Memorial Sloan Kettering Cancer Center Institutional review board (IRB) to be of low risk due to patients volunteering to undergo optical imaging with a radiopharmaceutical previously administered for standard of care diagnostics or therapy. Patients with any tumour or nodal metastases, existing or suspected, who were scheduled for routine clinical imaging or therapy using any of five radiotracers (^{18}F-FDG, $Na^{131}I$, ^{68}Ga-DOTATATE, ^{177}Lu-DOTATATE, or $^{223}RaCl_2$) were included in the study. The radionuclide administered was determined by their physician as part of their standard of care and CLI was generally performed within one hour of the scheduled scan. Imaging was conducted in an unblinded fashion, using previous scans to determine study eligibility and defining the region of interest for CLI. Patient eligibility was determined by the presence of disease in superficial lymph nodes by the subclavian vein, as well as deeper lesions such as in the bone, liver, and pancreatic or mesenteric metastases. The trial was designed to recruit 128 patients administered one of the five radiopharmaceuticals. Study exclusion criteria for the study included nyctophobia, claustrophobia, or skin blemishes or markings that could obscure transmitted CL. Bandages, medical staples, and sutures adjacent to known lesions as well as darker skin coloration were not subject to exclusion. The enclosure design required patients to be ambulatory and capable of communicating their well-being during the imaging session. Patient consent was re-obtained for each subsequent imaging session.

Procedures

Patients were informed about the study a few days before the scheduled appointment and approached for consent on the day of imaging upon arriving to the clinic. Consenting patients then underwent CLI after radiotracer injection in the hour before or immediately after their standard-of-care nuclear medicine scan or therapy administration. Patients were asked to sit as motionless as possible for a traditional white light photograph (anatomic

reference) followed by an up to 15-minute CL image with the imaging enclosure sealed from ambient light. The enclosure was opened/closed using double-layered lightproof black plastic curtains, which could be operated independently on two internal tracks that also served as light labyrinths to exclude external ambient stray photons. The fiberscope could be positioned around the patient with a three-axis mechanical arm and contains a cerrobend baffle at the lens to reduce radiation exposure to the fiberscope. Before imaging, patient imaging distance from the fiberscope was measured with a laser rangefinder for manual focus confirmation. Cerenkov images could be acquired with an open filter, maximizing all available light, or with one of four spectral filters capturing <500 nm, 500–550 nm, 550–600 nm, and >600 nm.

Cerenkov images were acquired with a specially sourced Andor iXon Ultra 897 EMCCD camera cooled to −80°C and set to electron multiplying mode with a gain of 300 and a pixel binning of either 4×4 or 8×8. Images were post-processed using an automated script (macro) in ImageJ comprised of standard plugins (Supplementary Fig. 11) to remove gamma strikes and fibre scintillation via outlier removal (median filtering).[52] Horizontal striping defects present in the system, vignetting and background noise were suppressed via the ImageJ bandpass FFT plugin[50]. Any remaining vignetting was removed via border cropping where vignetting effects are most prominent within the field of view. Smoothening was then applied before finally thresholding the image to display the top 5% of the grey values. Due to the inherent macroscale nature of clinical CLI and the induced aberrations due to light scatter and absorption in tissue, processing code was utilized to increase clarity and consistency in image acquisition as opposed to increasing spatial resolution. At this imaging scale, any reduction in spatial resolution by post processing is negligible in comparison to both the required on-sensor binning the light scatter by tissue and ultimately is outweighed by the resulting increase in light sensitivity. Additionally, the system is primarily designed to be used as an essentially binary detection method where CL is either present and elevated or not. If a patient reconsented to imaging at a later date, identical (as much as possible) distance, projection, and acquisition settings were repeated to allow intensity comparisons between sessions. Phantoms were used in the enclosure at various distances (0.66’–3’) and exposure times to determine the camera radiance intensity correlation and confirm camera settings for patient imaging before a new radiotracer was imaged (Supplementary Fig. 12).

Clinical scans (PET/CT, SPECT) used for correlation with CLI were obtained with permission from the MSKCC IRB. Clinical images were analysed for lesion depth to skin, size of lesion, and activity in the imaging region, as well as corresponding coronal, axial, or sagittal image slice to identify the radiotracer area avidity. Clinical PET and SPECT images used for analysis were taken on the same day as CLI, except for $^{223}RaCl_2$ images, which were compared to their previous bone scan (^{99m}Tc-MDP or ^{18}F PET). Four board-certified radiologists with nuclear medicine expertise (JG 15 years of experience; PC, 2 years of experience; AA, 3 years of experience; and PS, 4 years of experience) reviewed all the images from PET/CT or SPECT and CLI, knowing only the clinical diagnosis and radiotracer administered for each image pair.

Outcomes

Patients were informed during consent that participation in the Cerenkov fiberscope imaging trial did not affect their standard of care, though providing physicians could review the images if requested. Patients were free to exit from the study at any time.

Statistical analysis

Data and statistical analyses were performed using GraphPad Prism v7.0d (GraphPad Software, Inc.). Cerenkov intensity versus activity administered or known lesion depth was fit with a Spearman correlation. Spearman's rank and confidence intervals are provided in the Fig. 5 legend. Values in each figure represent two-tailed P-values.

Extended Data

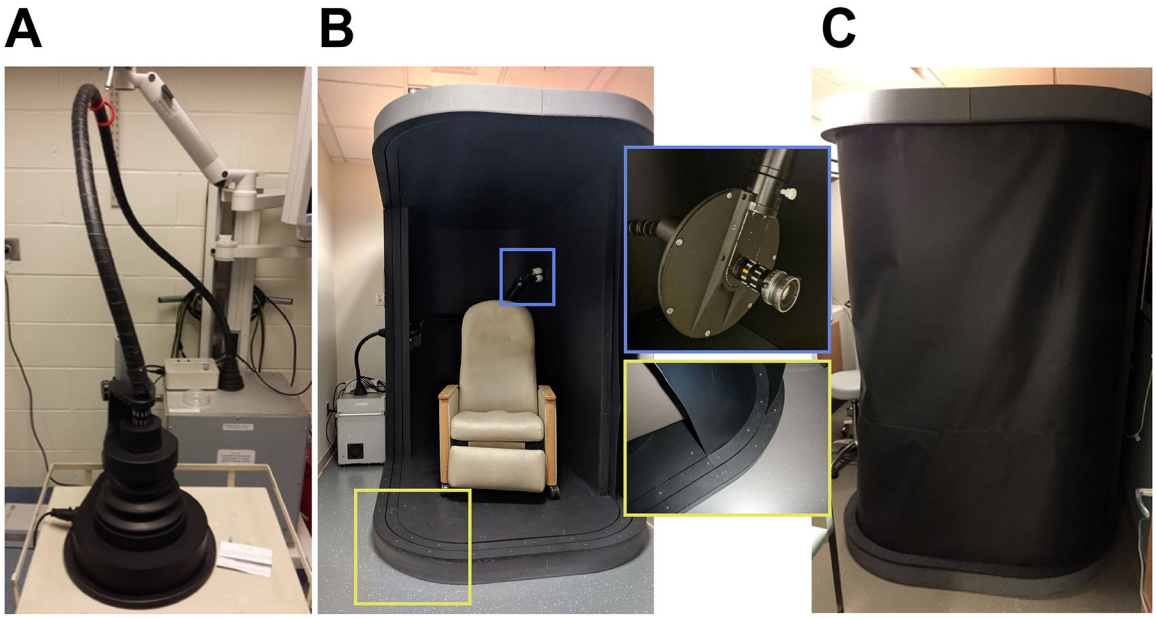

ED Fig. 1. Clinical Cerenkov imaging system based on the Lightpoint fiberscope design
A) The Cerenkov camera (Andor iXon Ultra 897 EMCCD, Andor Technology Ltd., Belfast, UK) enclosed in a lead shielded box (background) with a connecting fiberscope to a preclinical enclosure (foreground). **B)** Clinical enclosure (Lightpoint Medical Ltd., Chesham, UK) containing a reclining chair for patient imaging. The fiberscope (Lightpoint Medical Ltd., Chesham, UK) is installed through the rear of the enclosure opposite the dual track shroud system (red box inset). The fiberscope is held in place via a three-axis articulating arm containing a cerrobend baffle to reduce gamma and beta strikes to the fiber (green box inset). A 17 mm C-mount lens with an *f#* of 0.95 was used to collect CL (Xenon 0.95/17, Jos. Schneider Optische Werke GmbH, Bad Kreuznach, GM) **C)** Example of both shrouds deployed to prevent ambient light from reaching the patient during CLI.

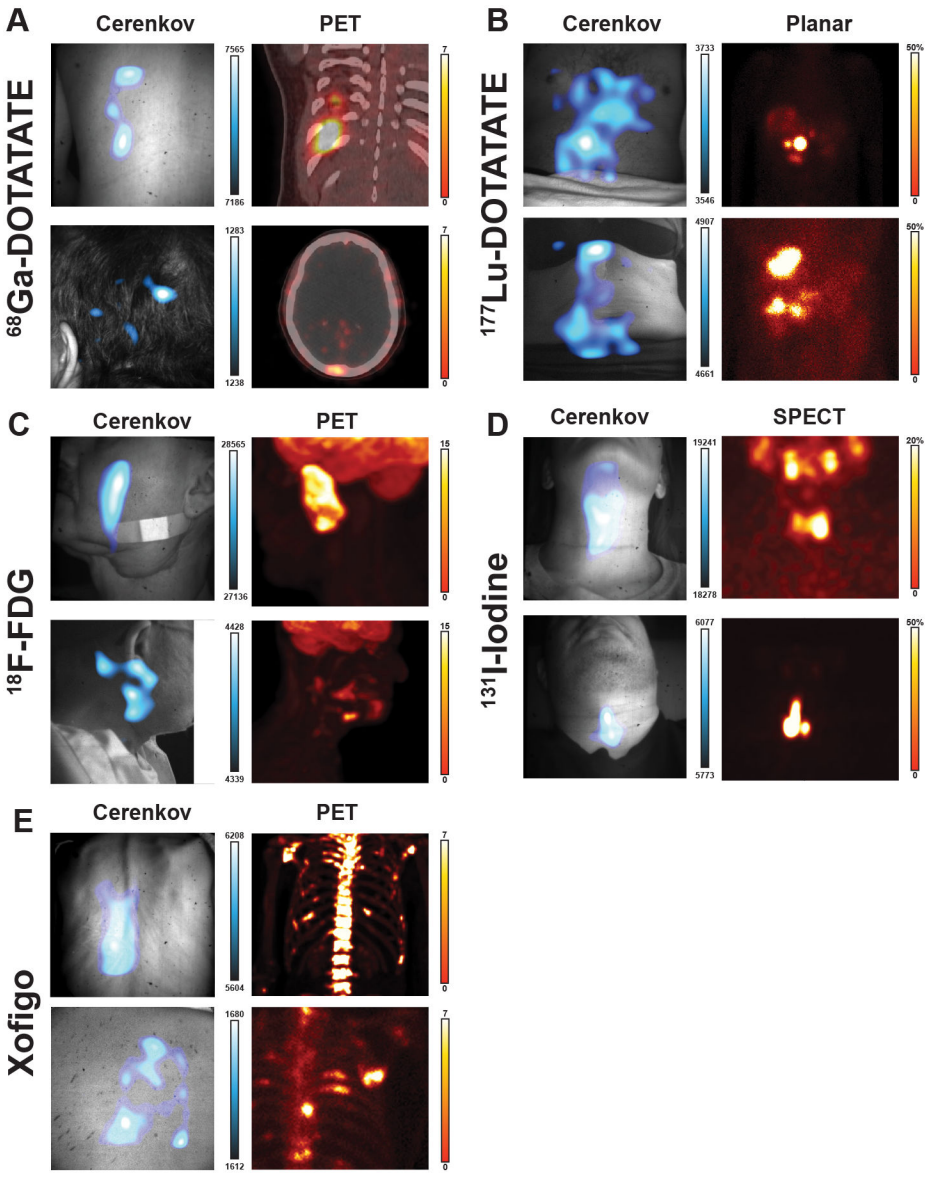

ED Fig. 2. Additional patient images by isotope showing the versatility of CCLI reflect the employed tracer and patient imaging location

A) Top, ^{68}Ga-DOTATATE CLI image shows three lesions on the posterior agree with the PET/CT, the presence on the posterior of a superficial lesion near the ribcage, directly above the spleen. Lesion discrepancy between PET and CLI is likely due to rib bone absorption. Bottom, a second patient has a prominent spot on their head in the CLI image which aligns with a lesion seen in the PET/CT in the occipital bone near the lamboid suture. B) Top, ^{177}Lu-DOTATATE CLI image shows a patient with the brightest spot below the liver with a secondary area near the patient midline below the Xiphoid Process. The main focal spot is in agreement with the planar scan the patient received prior showing one main lesion in a cluster of four below the liver near the patient midline. Bottom, CLI image of a second patient showing a focal region just above the Xiphoid Process with a secondary focal area to the patient's right abdomen in line with the navel. The corresponding planar image shows

two sets of lesions, one in the top of the right lobe as well as two lesions in the bottom of the right lobe of the liver. C) Top, ^{18}F-FDG CLI image shows a vertical focal signal in the cheek and not near the applied bandage. The corresponding PET image shows the most avid region by the zygomatic bone and nearly vertical with the patient. The physiologic uptake in the brain is not seen as it is both less intense and attenuated by the skull. Bottom, a second ^{18}F-FDG patient CLI image shows three clusters at the base of the jaw and around the ear. The corresponding PET scan shows three sets of avid tissue in the region in agreement with the CLI image, with the brightest lesion buried in the submandibular triangle. E) Top, ^{223}RaCl2 CLI image shown from the patients back that the main CLI intensity is to the left of the spine, near the liver. A prior ^{18}F scan from the previous month shows extensive uptake in the spine, suggesting the CLI intensity seen is distribution of ^{223}RaCl2 through the liver and not appreciable bone uptake. Bottom, CLI image showing a patient's right posterior to the left of the scapula from an elevated angle above the patient with three focal regions seen. The prior ^{18}F bone scan from the previous month shows uptake in the 4th and 5th ribs, alongside two focal lesions on either side. Here the CLI image shows potential agreement with the ^{18}F scan, though physiologic distribution via stomach and gastrointestinal tract confounds agreement.

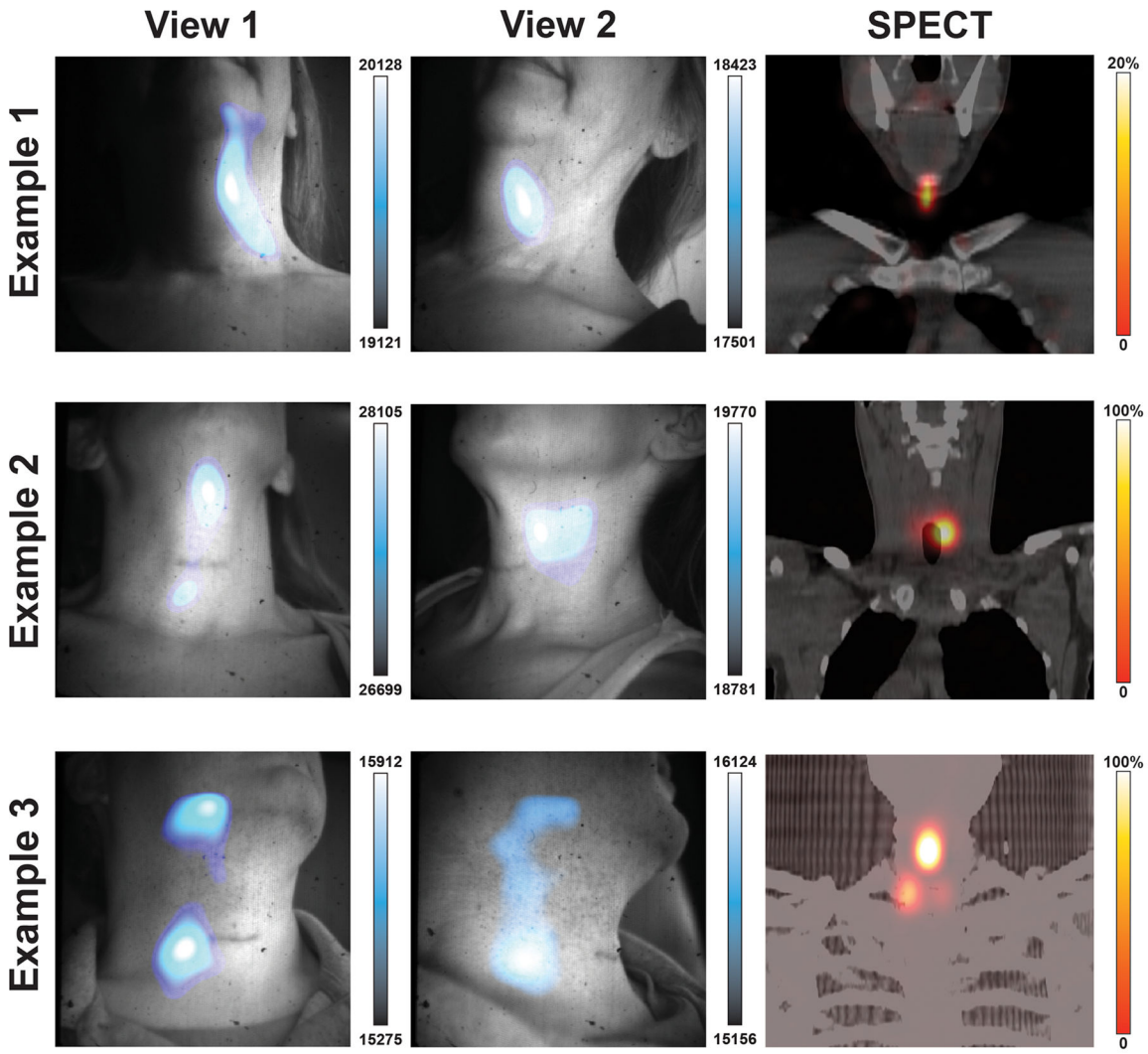

ED Fig. 3. Additional patient images with alternate CLI projections

^{131}I-Iodine patients were imaged head on and from the side. Example 1 shows images from two angles with CLI focal intensity in the patients left neck before the muscular triangle with corresponding SPECT image showing uptake near the submental triangle. In Example 2 CLI images show intensity regions below the submental triangle and before the submandibular triangle while the corresponding SPECT scan shows the iodine uptake to be located deeper in the neck below the submandibular triangle adjacent to the trachea. In Example 3, two focal regions of CLI are seen between projections with the reduction of the upper CLI region in View 2. The corresponding SPECT scan shows three lesions with the brightest lesion to the right of the patient midline and below the submental triangle. Here CLI shows in example 3 the most avid lesion in the midline, though the upper CLI spot appears to be an artifact that dissipated in the second view. Overall, the most iodine avid region in the field of view was where the most intense CLI signal was seen, with the exception of the artifact seen in View 1 of Example 3 which dissipated in View 2. Possible sources of artifact light include insufficient time (< 5 minutes) to let the light from the

patient and enclosure dissipate along with residual charge on the sensor, as well as patient movement.

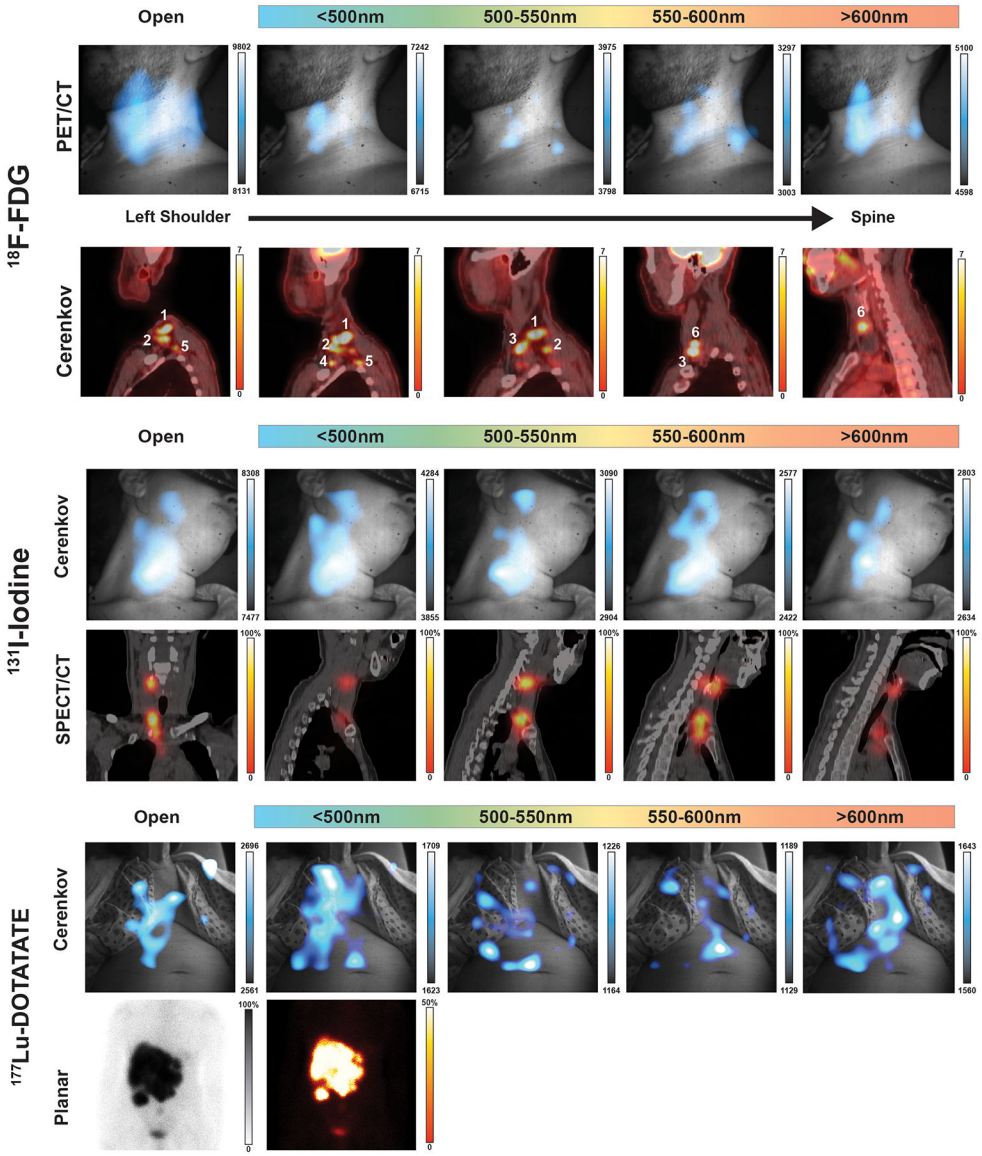

ED Fig. 4. Additional patient images imaged with filters

(Top) Complete filter set of patient in Figure 3. Here a representative patient has multifocal nodules in the subclavian vein, which cannot be completely separated with the installed short-pass and bandpass filters. The major lesions denoted as 1 and 3 can be seen in each filter but without the corresponding PET or CT the difference in CLI intensity does not meaningfully infer depth. **(Middle)** A patient with two thyroid nodules was imaged with each filter after receiving an adjuvant therapy dose of iodine-131, where the open and each filter image shows one main nodule towards the base of the neck. The upper thyroid nodule in the submandibular triangle is barely visible until the 600 nm bandpass filter, with little differentiation of CLI images with the 500nm short-pass and band pass filters

compared to the open filter image. **(Bottom)** In the ^{177}Lu-DOTATATE filter example a large multicomponent liver metastasis is seen in the planar image, yet a high degree of CLI intensity is seen on the patients' clothing though centered over the liver. The brightest CLI spot in the open and 500nm short-pass filter images are not avid areas in the planar scan, however the longer bandpass filters, and especially the 600nm long pass filter which best represents the planar scan. Together the filtering of light from CLI in patients is useful above 600nm where shorter wavelength filtering is troubled by a lack of definition between filters as well as high tissue absorption and scattering of any emitted CL.

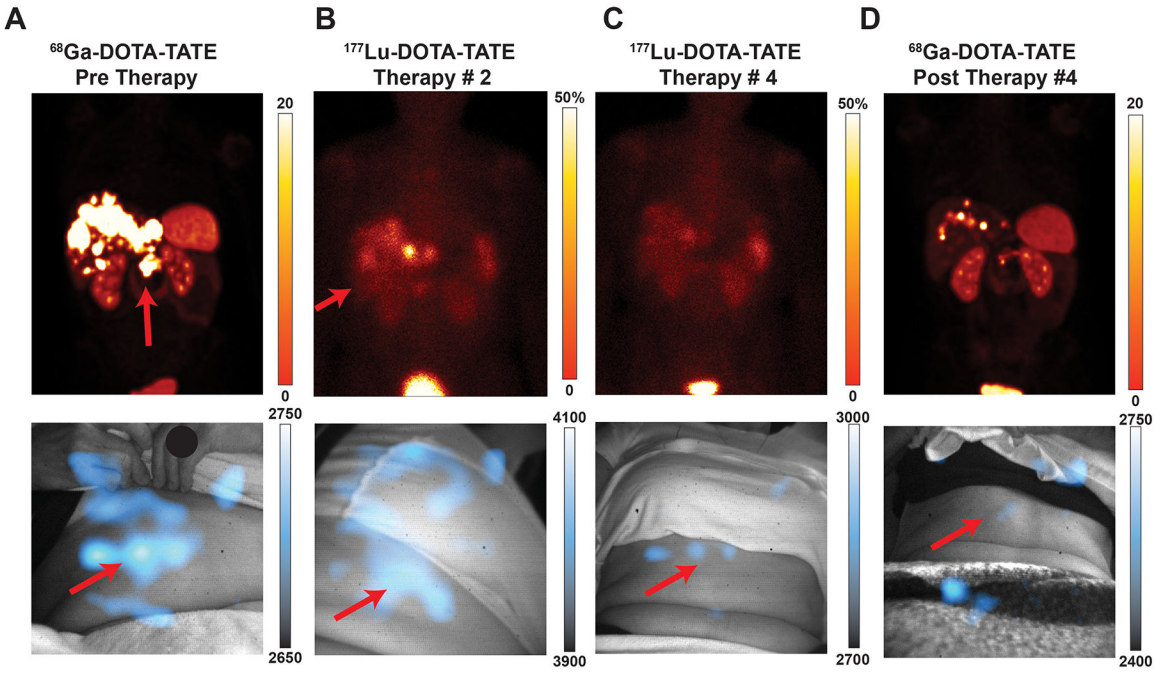

ED Fig. 5. Cerenkov luminescence images of ^{68}Ga/^{177}Lu-DOTATATE therapy with lower minimum CLI intensity to identify residual disease

Post therapy images show reduced uptake in the abdomen, though most intense regions remain where disease is present. Artifact light can be seen on clothing.

Supplementary Material

Refer to Web version on PubMed Central for supplementary material.

Acknowledgements

We are thankful to the 96 patients, who gave their time (some of them repeatedly) in moments of considerable stress to support our study. We are also grateful for the support of MSKCC's Molecular Imaging and Therapy Service, particularly from the service chief Dr. Heiko Schöder. This study is dedicated to Dr. Sanjiv Sam Gambhir, who encouraged us to think out of the box and to continue in our endeavours in this field. JG and DT were funded by NIH R01 CA18395305. We thank Lightpoint Medical, Ltd for the assembly of the CL camera and enclosure. This research was also funded in part through the NIH/NCI Cancer Center Support Grant P30 CA008748.

Competing interests

JG and DT are recipients of the NIH grant R01 CA18395305. DT and KV are employees of and have equity in Lightpoint Medical. The other authors declare no competing interests.

Data availability

The data generated and analysed during the study were funded by NIH R01CA18395305, and de-identified data can be made available by the corresponding author on reasonable request. The code used to process and overlay Cerenkov images is available from Zenodo at https://doi.org/10.5281/zenodo.6261583.

References

1. Organization, W. N. Radioisotopes in Medicine, < http://www.world-nuclear.org/information-library/non-power-nuclear-applications/radioisotopes-research/radioisotopes-in-medicine.aspx> (2020).
2. Organization, W. H. Cancer Fact Sheets, <https://www.who.int/news-room/fact-sheets/detail/cancer> (2018).
3. Organization, W. H. Global atlas of medical devices. 480 p. (World Health Organization, 2017).
4. Hricak H et al. Medical imaging and nuclear medicine: a Lancet Oncology Commission. The Lancet Oncology 22, e136–e172, doi:10.1016/s1470-2045(20)30751-8 (2021). [PubMed: 33676609]
5. Cutler CS et al. Global Issues of Radiopharmaceutical Access and Availability: A Nuclear Medicine Global Initiative Project. J Nucl Med 62, 422–430, doi:10.2967/jnumed.120.247197 (2021). [PubMed: 32646881]
6. Khan SH Cancer and positron emission tomography imaging in India: Vision 2025. Indian J Nucl Med 31, 251–254, doi:10.4103/0972-3919.190804 (2016). [PubMed: 27833308]
7. Páez D et al. Current Status of Nuclear Medicine Practice in Latin America and the Caribbean. J Nucl Med 56, 1629–1634, doi:10.2967/jnumed.114.148932 (2015). [PubMed: 26229143]
8. Buck AK et al. Economic evaluation of PET and PET/CT in oncology: evidence and methodologic approaches. J Nucl Med Technol 38, 6–17, doi:10.2967/jnmt.108.059584 (2010). [PubMed: 20197541]
9. d. P. Brambilla T Studies of adsorber materials for preparing 68Ge/68Ga generators, (2013).
10. Beattie BJ et al. Quantitative modeling of Cerenkov light production efficiency from medical radionuclides. PLoS One 7, e31402, doi:10.1371/journal.pone.0031402 (2012). [PubMed: 22363636]
11. Shaffer TM, Pratt EC & Grimm J Utilizing the power of Cerenkov light with nanotechnology. Nat Nanotechnol 12, 106–117, doi:10.1038/nnano.2016.301 (2017). [PubMed: 28167827]
12. Das S, Thorek DL & Grimm J Cerenkov imaging. Adv Cancer Res 124, 213–234, doi:10.1016/B978-0-12-411638-2.00006-9 (2014). [PubMed: 25287690]
13. Pratt EC, Shaffer TM, Zhang Q, Drain CM & Grimm J Nanoparticles as multimodal photon transducers of ionizing radiation. Nature Nanotechnology 13, 418–426, doi:10.1038/s41565-018-0086-2 (2018).
14. Zhang R, Glaser AK, Gladstone DJ, Fox CJ & Pogue BW Superficial dosimetry imaging based on Cerenkov emission for external beam radiotherapy with megavoltage x-ray beam. Med Phys 40, 101914, doi:10.1118/1.4821543 (2013). [PubMed: 24089916]
15. Czupryna J et al. Cerenkov-Specific Contrast Agents for Detection of pH In Vivo. Journal of Nuclear Medicine 56, 483–488, doi:10.2967/jnumed.114.146605 (2015). [PubMed: 25655631]
16. Thorek DL, Ogirala A, Beattie BJ & Grimm J Quantitative imaging of disease signatures through radioactive decay signal conversion. Nat Med 19, 1345–1350, doi:10.1038/nm.3323 (2013). [PubMed: 24013701]
17. Robertson R et al. Optical imaging of Cerenkov light generation from positron-emitting radiotracers. Phys Med Biol 54, N355–365, doi:10.1088/0031-9155/54/16/N01 (2009). [PubMed: 19636082]
18. Boschi F et al. In vivo (1)(8)F-FDG tumour uptake measurements in small animals using Cerenkov radiation. Eur J Nucl Med Mol Imaging 38, 120–127, doi:10.1007/s00259-010-1630-y (2011). [PubMed: 20882278]

19. Thorek DL, Riedl CC & Grimm J Clinical Cerenkov luminescence imaging of (18)F-FDG. J Nucl Med 55, 95–98, doi:10.2967/jnumed.113.127266 (2014). [PubMed: 24078721]
20. Spinelli AE et al. 3 (SPIE).
21. Hu H et al. Feasibility study of novel endoscopic Cerenkov luminescence imaging system in detecting and quantifying gastrointestinal disease: first human results. Eur Radiol 25, 1814–1822, doi:10.1007/s00330-014-3574-2 (2015). [PubMed: 25577521]
22. Tamura R, Pratt EC & Grimm J Innovations in Nuclear Imaging Instrumentation: Cerenkov Imaging. Seminars in Nuclear Medicine, doi:10.1053/j.semnuclmed.2018.02.007.
23. Gioux S et al. in Molecular-Guided Surgery: Molecules, Devices, and Applications IV (2018).
24. Ciarrocchi E et al. Performance evaluation of the LightPath imaging system for intra-operative Cerenkov luminescence imaging. Physica Medica 52, 122–128 (2018). [PubMed: 30139600]
25. Olde Heuvel J et al. Performance evaluation of Cerenkov luminescence imaging: a comparison of (68)Ga with (18)F. EJNMMI Phys 6, 17, doi:10.1186/s40658-019-0255-x (2019). [PubMed: 31650365]
26. Grootendorst MR, Cariati M, Kothari A, Tuch DS & Purushotham A Cerenkov luminescence imaging (CLI) for image-guided cancer surgery. Clin Transl Imaging 4, 353–366, doi:10.1007/s40336-016-0183-x (2016). [PubMed: 27738626]
27. Grootendorst MR et al. Intraoperative Assessment of Tumor Resection Margins in Breast-Conserving Surgery Using 18F-FDG Cerenkov Luminescence Imaging: A First-in-Human Feasibility Study. J Nucl Med 58, 891–898, doi:10.2967/jnumed.116.181032 (2017). [PubMed: 27932562]
28. Song T et al. A Novel Endoscopic Cerenkov Luminescence Imaging System for Intraoperative Surgical Navigation. Molecular Imaging 14, doi:10.2310/7290.2015.00018 (2015).
29. Kothapalli S-R, Liu H, Liao JC, Cheng Z & Gambhir SS Endoscopic imaging of Cerenkov luminescence. Biomedical Optics Express 3, 1215–1225, doi:10.1364/BOE.3.001215 (2012). [PubMed: 22741069]
30. Moses WW Fundamental limits of spatial resolution in PET. Nuclear Instruments and Methods in Physics Research Section A: Accelerators, Spectrometers, Detectors and Associated Equipment 648, S236–S240, doi:10.1016/j.nima.2010.11.092 (2011).
31. Flux GD Imaging and dosimetry for radium-223: the potential for personalized treatment. Br J Radiol 90, 20160748, doi:10.1259/bjr.20160748 (2017).
32. Costa DN et al. Diagnostic Utility of a Likert Scale Versus Qualitative Descriptors and Length of Capsular Contact for Determining Extraprostatic Tumor Extension at Multiparametric Prostate MRI. AJR Am J Roentgenol 210, 1066–1072, doi:10.2214/AJR.17.18849 (2018). [PubMed: 29489410]
33. Koksel Y et al. Utility of Likert scale (Deauville criteria) in assessment of Chemoradiotherapy response of primary oropharyngeal squamous cell Cancer site. Clinical Imaging 55, 89–94, doi:10.1016/j.clinimag.2019.01.007 (2019). [PubMed: 30771643]
34. Phelps AS et al. Pairwise comparison versus Likert scale for biomedical image assessment. AJR Am J Roentgenol 204, 8–14, doi:10.2214/AJR.14.13022 (2015). [PubMed: 25539230]
35. Rosenkrantz AB et al. Prostate Cancer Localization Using Multiparametric MR Imaging: Comparison of Prostate Imaging Reporting and Data System (PI-RADS) and Likert Scales. Radiology 269, 482–492, doi:10.1148/radiol.13122233 (2013). [PubMed: 23788719]
36. Carrasquillo JA et al. Phase I pharmacokinetic and biodistribution study with escalating doses of (2)(2)(3)Ra-dichloride in men with castration-resistant metastatic prostate cancer. Eur J Nucl Med Mol Imaging 40, 1384–1393, doi:10.1007/s00259-013-2427-6 (2013). [PubMed: 23653243]
37. Jacques SL Optical properties of biological tissues: a review. Physics in Medicine & Biology 58, R37 (2013). [PubMed: 23666068]
38. Abbaci M, Conversano A, De Leeuw F, Laplace-Builhe C & Mazouni C Near-infrared fluorescence imaging for the prevention and management of breast cancer-related lymphedema: A systematic review. Eur J Surg Oncol 45, 1778–1786, doi:10.1016/j.ejso.2019.06.009 (2019). [PubMed: 31221460]
39. Alander JT et al. A review of indocyanine green fluorescent imaging in surgery. Int J Biomed Imaging 2012, 940585, doi:10.1155/2012/940585 (2012).

40. Vahrmeijer AL, Hutteman M, van der Vorst JR, van de Velde CJ & Frangioni JV Image-guided cancer surgery using near-infrared fluorescence. Nat Rev Clin Oncol 10, 507–518, doi:10.1038/nrclinonc.2013.123 (2013). [PubMed: 23881033]
41. Nagaya T, Nakamura YA, Choyke PL & Kobayashi H Fluorescence-Guided Surgery. Front Oncol 7, 314, doi:10.3389/fonc.2017.00314 (2017). [PubMed: 29312886]
42. van Leeuwen FWB, Hardwick JCH & van Erkel AR Luminescence-based Imaging Approaches in the Field of Interventional Molecular Imaging. Radiology 276, 12–29, doi:10.1148/radiol.2015132698 (2015). [PubMed: 26101919]
43. Glaser AK, Zhang R, Andreozzi JM, Gladstone DJ & Pogue BW Cherenkov radiation fluence estimates in tissue for molecular imaging and therapy applications. Phys Med Biol 60, 6701–6718, doi:10.1088/0031-9155/60/17/6701 (2015). [PubMed: 26270125]
44. Ciarrocchi E & Belcari N Cerenkov luminescence imaging: physics principles and potential applications in biomedical sciences. EJNMMI Phys 4, 14, doi:10.1186/s40658-017-0181-8 (2017). [PubMed: 28283990]
45. LaRochelle EPM, Shell JR, Gunn JR, Davis SC & Pogue BW Signal intensity analysis and optimization for in vivo imaging of Cherenkov and excited luminescence. Phys Med Biol 63, 085019, doi:10.1088/1361-6560/aab83b (2018).
46. Fragoso Costa P et al. Early Results of Intraoperative68Ga-PSMA Cerenkov Luminescence Imaging in Radical Prostatectomy. Journal of Nuclear Medicine 60, 658 (2019).
47. Bagguley D, Cumberbatch M, Lawrentschuk N & Murphy DG Cerenkov Luminescence Imaging for Surgical Margins in Radical Prostatectomy: A Surgical Perspective. J Nucl Med 61, 1498–1499, doi:10.2967/jnumed.120.243303 (2020). [PubMed: 32591492]
48. Darr C et al. Intraoperative (68)Ga-PSMA Cerenkov Luminescence Imaging for Surgical Margins in Radical Prostatectomy: A Feasibility Study. J Nucl Med 61, 1500–1506, doi:10.2967/jnumed.119.240424 (2020). [PubMed: 32060212]
49. Darr C et al. First-in-man intraoperative Cerenkov luminescence imaging for oligometastatic prostate cancer using (68)Ga-PSMA-11. Eur J Nucl Med Mol Imaging, doi:10.1007/s00259-020-04778-y (2020).
50. Walter J FFT-filter. Available at: http://rsb.info.nih.gov/ij/plugins/fft-filter.html. (2001).
51. Hachadorian R et al. Imaging radiation dose in breast radiotherapy by x-ray CT calibration of Cherenkov light. Nature communications 11, 1–9 (2020).
52. Schindelin J et al. Fiji: an open-source platform for biological-image analysis. Nat Methods 9, 676–682 (2012). [PubMed: 22743772]
53. Gill RK, Mitchell GS & Cherry SR Computed Cerenkov luminescence yields for radionuclides used in biology and medicine. Phys Med Biol 60, 4263–4280, doi:10.1088/0031-9155/60/11/4263 (2015). [PubMed: 25973972]

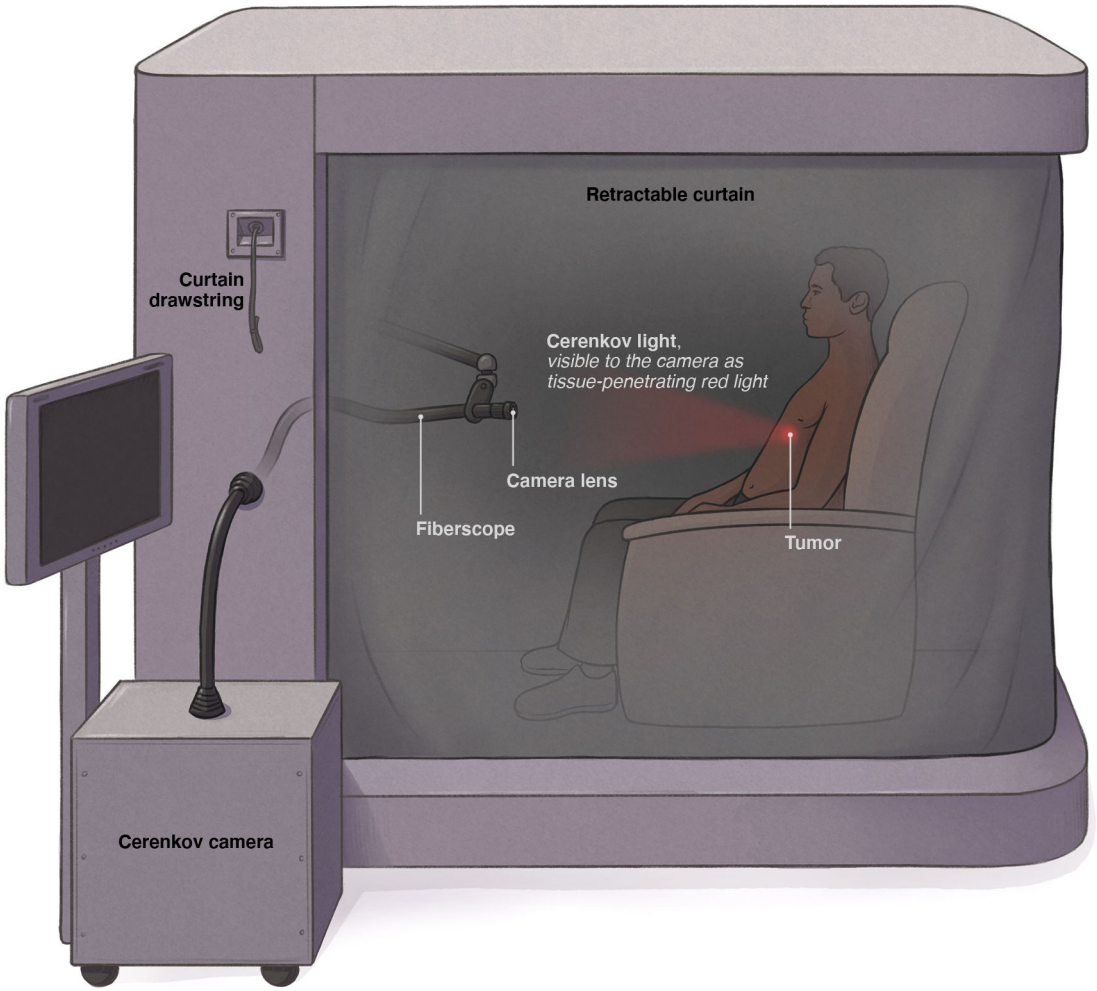

Fig. 1 |. Clinical Cerenkov Fiberscope setup with lightproof enclosure for patient imaging.
Cerenkov luminescence is weak but measurable light emanating from alpha- or beta-emitting radionuclides used in nuclear imaging and therapy. After receiving a radiotracer, the patient is placed inside the lightproof enclosure for imaging for up to 15 minutes. The camera is placed outside of the enclosure and connected with relay optics at the proximal end of the bundle (inside the box) in addition to the fiberscope and a fast f~0.95 lens, the Cerenkov image from the patient can be recorded outside of the enclosure. Inside the enclosure the fiberscope can easily be positioned to the correct orientation to the patient with the three-axis articulating arm as well as shielded with a cerrobend baffle (Extended Data Fig. 1). As tissue highly absorbs and scatters ultraviolet and blue weighted light, the majority of the emitted CLI will be in the red part of the visible spectrum[11].

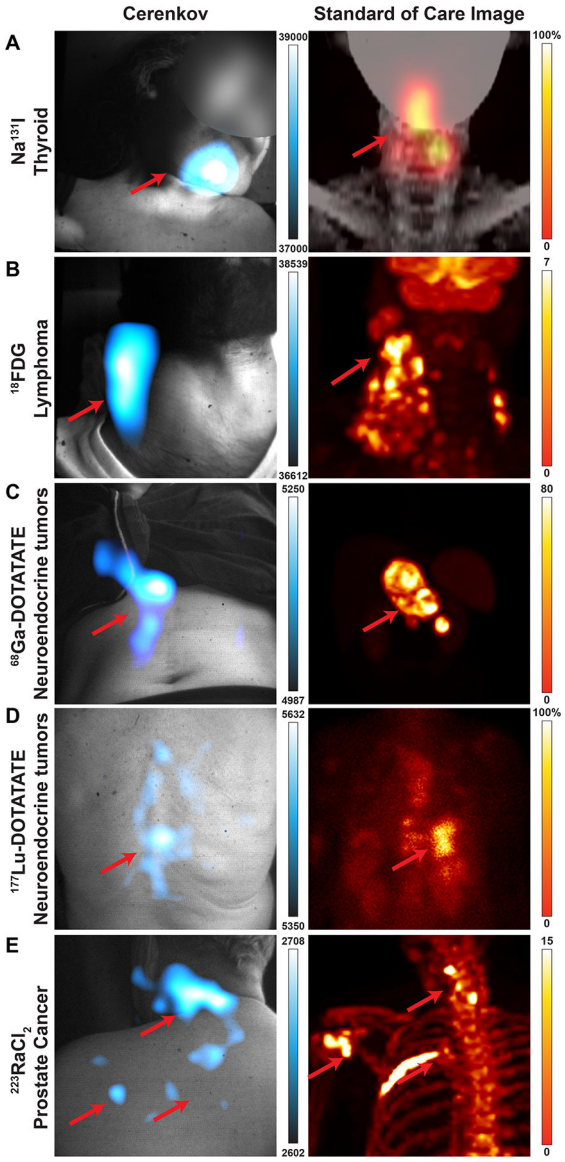

Fig. 2 |. Representative patients by isotope for fiberscope Cerenkov luminescence imaging. Cerenkov luminescence images of the patients (left) compared to their standard-of-care PET or SPECT/planar scan (right). Brightest Cerenkov luminescence imaging regions align with the most avid regions. As Cerenkov luminescence imaging is optical, avid lesions overlaid by tissue will appear dimmer than similarly avid lesions closer to the surface. **a**, 38-year-old woman diagnosed with papillary thyroid cancer, tall cell variant, treated with total thyroidectomy and left lateral neck dissection underwent adjuvant ^{131}I therapy. CL images were obtained after treatment with 144 mCi (5.3 GBq) of ^{131}I, which showed radiopharmaceutical uptake in the thyroid bed. CL image, false colorized by Cyan Hot, shows focal uptake in the thyroid bed as seen on the SPECT scan. **b**, 33-year-old man diagnosed with classic Hodgkin's lymphoma, nodular sclerosis type, in study for initial staging received ~12 mCi (0.4 GBq) of ^{18}F-FDG. ^{18}F-FDG PET/CT shows multiple hypermetabolic cervical, thoracic, and upper abdominal adenopathy. CLI identified a single

large focal area in the right neck and displays as one region due to scattering of light and post-processing smoothing. Most avid disease in the right neck is seen in both CLI and PET maximum intensity projections (MIPs) in the mid neck, while less avid disease is seen down the right neck to the clavicle. **c**, 41-year-old woman diagnosed with well-differentiated pancreatic neuroendocrine tumour in study for consideration of PRRT. Baseline ^{68}Ga-DOTATATE PET/CT delineates intense DOTATATE-avid upper abdominal adenopathy. CLI of the abdomen shows the most avid region is the tumour, though some artifacts on clothing were observed near the tumour and could be due to scattering, reflections, or patient movement. Furthermore, the presence of clothing and the rib cage likely attenuates or blocks CLI from the upper part of the lesion, leaving the central and lower part of the lesion to appear the brightest. From the angle imaged, the lesion appears on the right of the patient's midline, though the PET image shows the lesion traverses the midline. **d**, 74-year-old woman diagnosed with well-differentiated small bowel neuroendocrine tumour metastatic to the liver, nodes, and spine on treatment with ^{177}Lu-DOTATATE. After the first cycle of ^{177}Lu-DOTATATE, 2D planar image shows radiopharmaceutical uptake in the liver and thoracic and abdominopelvic nodes, as well as the spine, while CLI from the posterior shows focal activity on the spine, which may mean the patient shifted slightly during imaging since the most avid lesion in the planar image is just right of the spine. **e**, 64-year-old man diagnosed with metastatic prostate cancer in the bone underwent treatment with ^{223}Ra therapy, cycle four out of six. From prior ^{18}F scans, radiopharmaceutical uptake was observed in the pelvic bone and fourth left rib, as well as degenerative lesions in the cervical spine. CL was focused on the degenerative lesions in the cervical spine from a posterior position. CLI was also observed in the shoulder and posterior left 4th rib. CLI from the posterior rib was not likely seen due to the overlaid scapula and rhomboid muscle which would attenuate CL. Here, CL could directly image ^{223}Ra uptake without a subsequent ^{18}F bone scan or rely on the 1% gamma emissions from ^{223}Ra[31]. As with ^{223}Ra and ^{18}F imaging, physiologic distribution and degenerative lesion uptake complicates a potential diagnosis by imaging alone. Colour bars: CLI image intensity represents 16-bit grey value range, for **a**, SPECT image is scaled to 100% and **d**, 2D planar image is scaled to 100% of maximum image count. Standard of care images **b**, **c**, and **e** PET images are presented as maximum intensity projections and scaled to 0–7, 0–80, and 0–15 SUV, respectively.

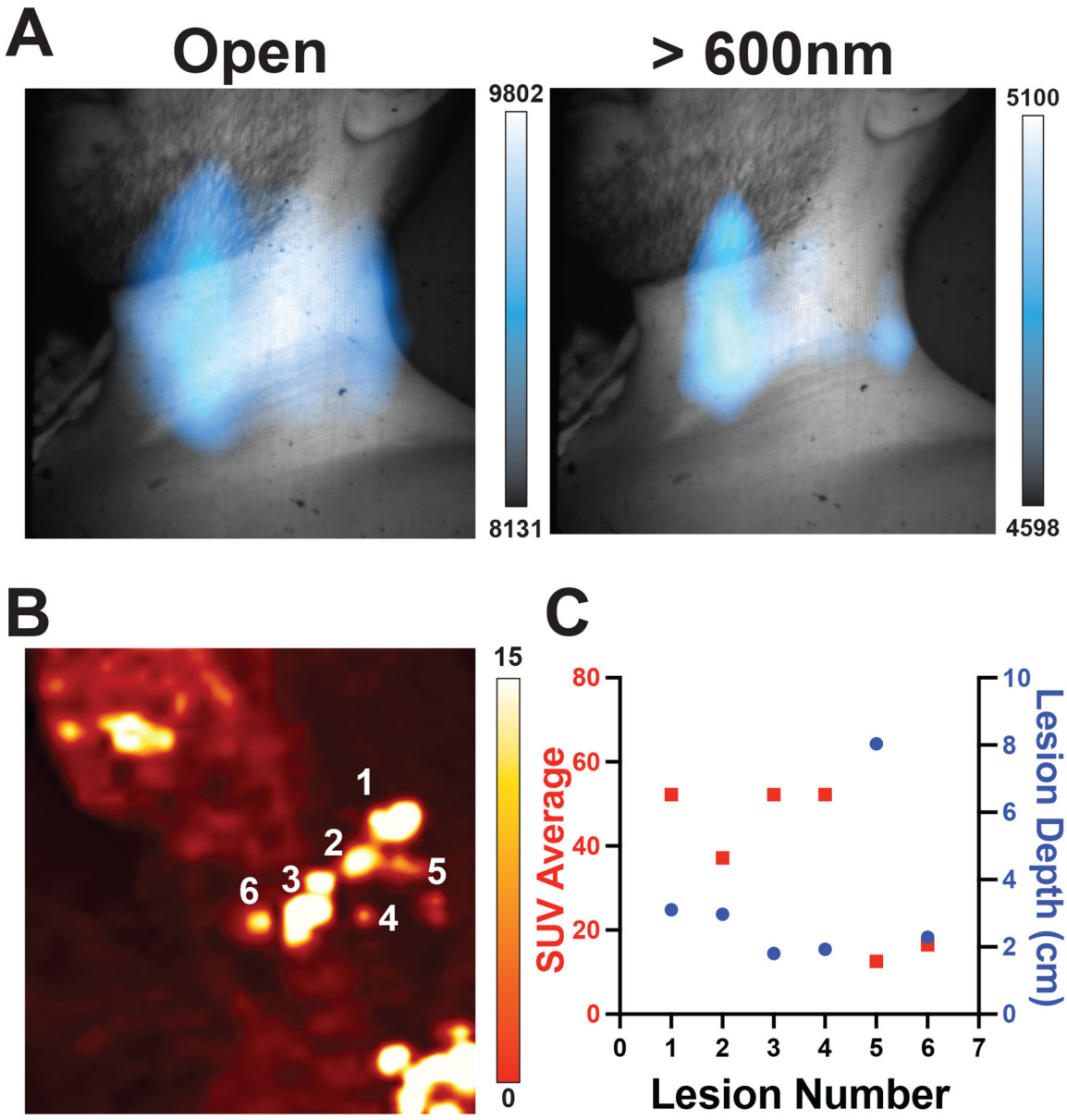

Fig. 3 |. Cerenkov luminescence imaging improved with filtering wavelengths above 600nm.
a, Applying a 600nm long pass filter to a patient with multiple nodes of disease produced clearer localization of lesions than the open filter alone. Deeper lesions could only be identified by CLI intensity if both the CT and the PET SUV were known for each major lesion. Here a representative patient has multifocal nodules in the subclavian vein, which cannot be completely separated due the high degree of scattering and absorption of light in tissue, with no differentiation with filters below 600nm (Extended Data Fig. 4). Of the CL filtered images, the 600nm bandpass was the brightest, confirming the majority of light emitted from the patient was red shifted. Mapping each lesion depth by PET/CT in **b** shows lesions reside between 1 and 8 cm from the patient's front with **c** SUVs between 20 and 55. By combining the SUV intensity with the lesion depth, lesions 1 and 3 are similarly ^{18}F-FDG avid but lesion 3 is closer to the surface, and in the 600nm long pass image lesion

3 is identifiable and notably brighter in CLI intensity. Lesion 2 might be visible, but with the degree of scattering and absorption present in the tissue it would be hard to identify until after the removal of lesions 1 and 3. Colour bars: CLI image intensity represents 16-bit grey value range, PET images are presented transversal images scaled to 0–7 SUV, while for **b** maximum intensity projection is scaled to 0–15 SUV to emphasize less avid lesions, and values obtained from standard PET/CT analysis available hospital-wide in the General Electric (GE) Picture Archiving and Communication System (PACS) for lesion depth and average SUV.

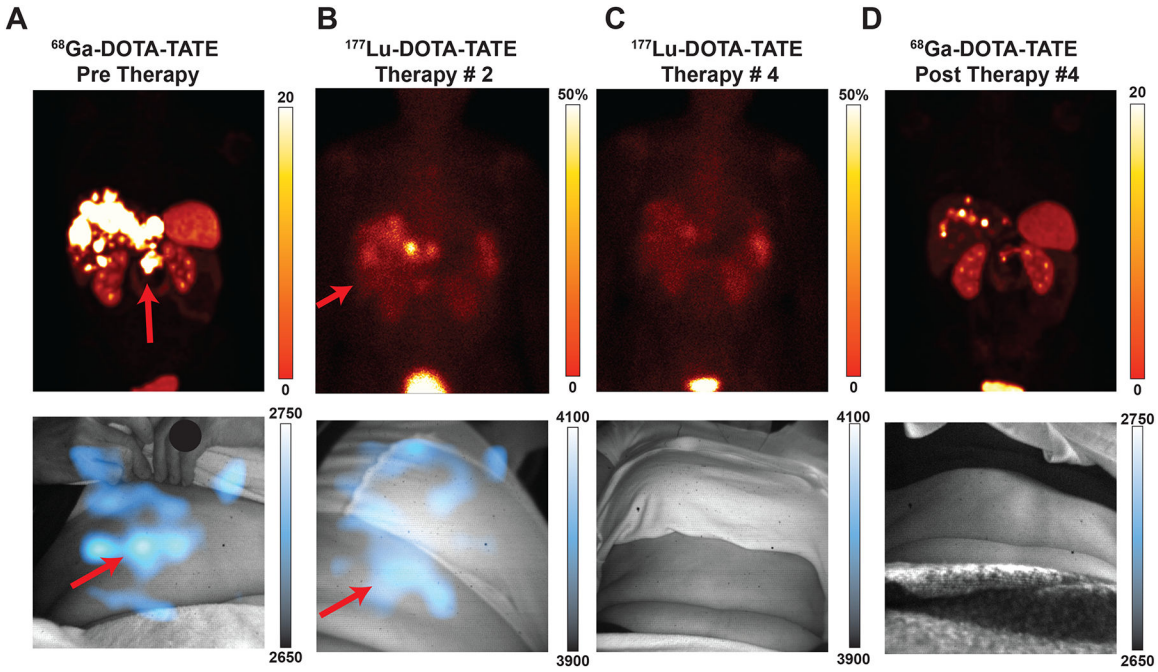

Fig. 4 |. CLI for monitoring therapy over successive imaging sessions.

All images presented with the initial CLI image intensity range for the given radiotracer. Min/max values can be found in Extended Data Fig. 5 for more precise disease monitoring. Intensities reported as the following: PET reported as SUV; planar SPECT and CL represented as pixel intensity. A 58-year-old woman diagnosed with well-differentiated pancreatic neuroendocrine tumour metastatic to the liver, on treatment with ^{177}Lu-DOTATATE peptide receptor radionuclide therapy (PRRT). Baseline ^{68}Ga-DOTATATE PET/CT (**Top Left**) Fused PET/CT coronal orientation delineates DOTATATE-avid tumour in the pancreatic body and multiple liver metastases. CLI of the patient immediately post PET/CT scan (**a Bottom**) shows a central abdominal lesion with scattering from liver metastases which are occluded in the liver and partially under the rib cage. After the first cycle of PRRT, a 2D planar image (**b Top**) shows the ^{177}Lu-DOTATATE uptake within the liver and pancreatic tumour. CL image of the abdomen, albeit at a different angle as the operator moves the fiberscope into place and patients can sit down differently, correlates ^{177}Lu-DOTATATE in the liver (**b Bottom**). After the third cycle of PRRT, the 2D planar image (**c Top**) shows marked reduction in radiopharmaceutical uptake in the pancreas and liver. Corresponding CL image (**c Bottom**) shows no clear CL signal when set to the intensity in b. At completion of the PRRT cycles, a diagnostic scan with ^{68}Ga-DOTATATE PET/CT (**d Top**) delineates a marked reduction in DOTATATE uptake with the pancreatic tumour and resolved uptake in the liver metastases. CLI of the patient post-PET/CT (**d Bottom**) windowed to the initial diagnostic scan **a** shows no appreciable CL signal. Comparing initial DOTATATE scans to subsequent images through one year of therapy, patient disease burden has significantly resolved (**Top**) and Cerenkov images show a reduction in radiotracer present as well, corroborating disease reduction. Subsequent images are matched to prior CL images for distance, acquisition time, binning, with projection matches as best as possible whilst ensuring patient comfort. Colour bars: CLI image

intensity represents 16-bit grey value range, for **a**, and **d**, PET images are presented as maximum intensity projections and scaled to 0–20 SUV, while for **b**, and **c**, 2D planar images are shown representing 50% maximum intensity (bladder).

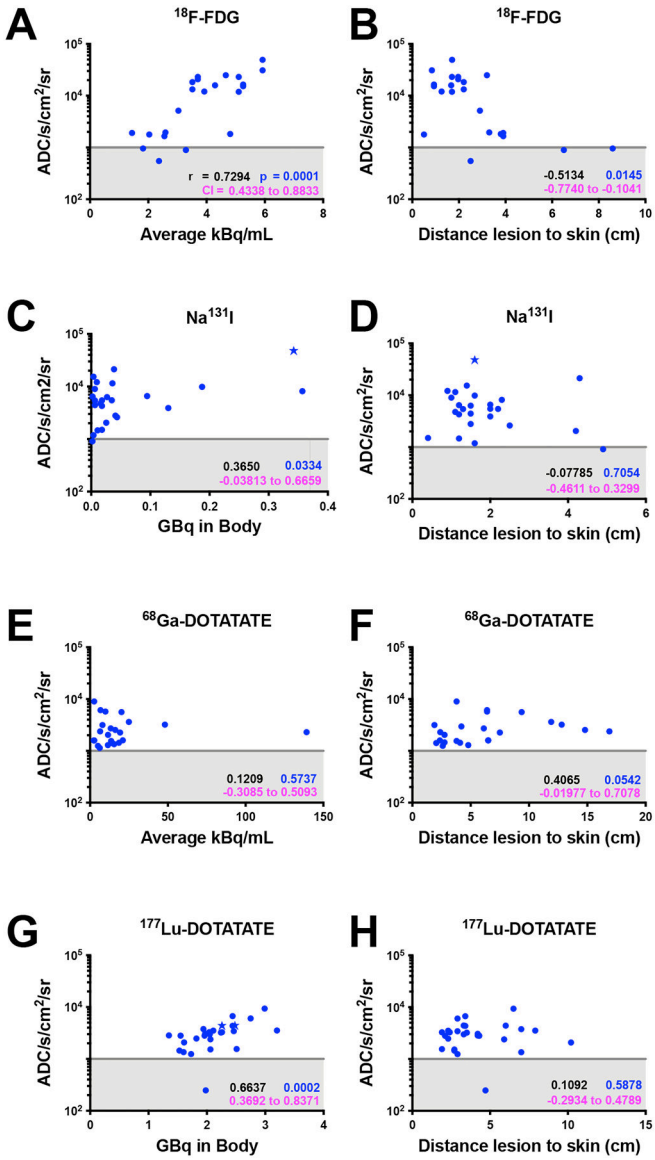

Fig. 5 |. CL intensity analysis of patient images correlated with the same-day, standard-of-care scan activity concentration or mCi in body or lesion depth as determined by CT.

CL units in analogue to digital counts (ADC) s^{-1} cm^{-2} sr^{-1}. Gray line represents the apparent limit of detection based upon the dark charge of the camera sensor, scattering and absorption of light, and the fiberscope optics. Star-shaped datapoints represent Black or African American patients. Spearman correlations in **a**, **b**, **c**, and **g** are significant whereas others did not achieve significance for the patients imaged. **a-h**, Spearman *r* values are in black, CI values in magenta, and *P*-values in blue.

Table 1 |

Radiotracers and details of accrual for IRB 17–538 specifying range of radiotracer administered and number of patient imaging sessions accrued at the time of writing.

Details reflect range of administered activity to the patient and computed Cerenkov light based on ([43,53]).

Radio-pharmaceutical	Indication	Clinical imaging mode	Typical dose, mCi (GBq)	Cerenkov light generated by isotope (photons/decay)[43,53]	Total possible Cerenkov light at injection (photons/second) × 10^9	Number of patient imaging sessions
$Na^{131}I$	Thyroid cancer adjuvant therapy	SPECT	27–200 (1.0–7.4)	0.669	5.0	25
^{18}F-FDG	General disease staging	PET	10–14.9 (0.37–0.55)	1.32	0.7	20
^{68}Ga-DOTATATE	Neuroendocrine PET imaging	PET	4.4–5.5 (119–149)	33.9	6.3	28
^{177}Lu-DOTATATE	Neuroendocrine radiotherapy	SPECT	188–200 (6.9–7.4)	0.141	1.0	26
$^{223}RaCl_2$	Metastatic castration-resistant prostate cancer therapy	None (separate PET or SPECT scan)	0.091–0.177 (0.0033–0.0065)	28.0104 (with daughters)	0.2	7

Table 2 |

Likert scoring summary for all Cerenkov luminescence imaging patients by administered radiopharmaceutical.

Individual counts and percentages (%) reflect Likert scores by radiopharmaceutical imaged. Likert scores shown are averages from four radiologists. Likert scores: 1- strongly disagree with correlation, 2- disagree with correlation, 3- intermediate or neutral correlation, 4- agree with correlation, 5- highly agree with correlation.

Score	^{18}F-FDG	Na^{131}I	^{68}Ga-DOTATATE	^{177}Lu-DOTATATE	^{223}RaCl$_2$
# (%)	20 (19)	25 (24)	28 (26)	26 (25)	7 (7)
5	0 (0)	0 (0)	0 (0)	0 (0)	0 (0)
4	8 (40)	9 (36)	3 (11)	5 (19)	0 (0)
3	7 (35)	11 (44)	22 (79)	16 (62)	5 (71)
2	3 (15)	4 (16)	3 (11)	3 (12)	2 (29)
1	2 (10)	1 (4)	0 (0)	2 (8)	0 (0)
4–5	8 (40)	9 (36)	3 (11)	5 (19)	0 (0)
3–5	15 (75)	20 (80)	25 (89)	21 (81)	5 (71)
1–2	5 (25)	5 (20)	3 (11)	5 (19)	2 (29)